Available online at www.sciencedirect.com

ScienceDirect

journal homepage: www.elsevier.com/locate/he

Hydrogen production from ethanol with low carbon monoxide generation in a one-pot reaction with iron oxides as catalysts

María F. Rochetti Yharour [a], *Nicolás A. Fellenz* [b], *Ana M. Alvarez* [a], *Jose F. Bengoa* [a,*], *Norma G. Gallegos* [a], *María V. Cagnoli* [a], *Sergio G. Marchetti* [a]

[a] *CINDECA, Fac. Cs. Exactas, Fac. Ingeniería, U.N.L.P., CIC, CONICET, Calle 47 No 257, 1900 La Plata, Argentina*
[b] *Universidad Nacional de Rio Negro, Sede Atlántica, Belgrano 526, 8500 Viedma, Rio Negro, Argentina*

ARTICLE INFO

Article history:
Received 13 March 2014
Received in revised form
19 May 2014
Accepted 12 June 2014
Available online 12 July 2014

Keywords:
Hydrogen production with low CO content
Ethanol hydrotreatment
Magnetite catalyst

ABSTRACT

Bulk γ-Fe_2O_3 (maghemite) and Fe_3O_4 (magnetite) were synthesized with Fe(III) hydroxyacetate as an intermediate during the preparation step. The fresh and used catalysts were characterized by X-ray diffraction, N_2 adsorption at 77 K, Mössbauer spectroscopy at 298 K, diffuse-reflectance spectroscopy, and thermogravimetric analysis. The solids were used as catalysts in the ethanol hydrotreatment within the range of 673–758 K. The catalysts showed a satisfactory selectivity for H_2 and an especially low CO production. These activities and selectivities were analyzed in conjunction with the structural properties of the oxides. Magnetite seemed to be a more appropriate catalyst than maghemite since the latter was converted into magnetite at reaction temperatures higher than 713 K because of the reducing atmosphere.

Copyright © 2014, Hydrogen Energy Publications, LLC. Published by Elsevier Ltd. All rights reserved.

Introduction

Energy surrounds us in all aspects of life and the ability to harness and use that resource for constructive ends—and as economically as possible—is the current challenge of society. Fossil fuels have been the energy source up to the present, to produce heat and electricity upon oxidative combustion. In this reaction, one of the by-products obtained is CO_2, which contributes to the atmospheric greenhouse effect. Researchers worldwide are seeking alternative energy sources to supplant the use of nuclear and fossil-fuel-based energies. Therefore any advance in sustainable development must gradually incorporate renewable energy sources to avoid the consumption of nonrenewable natural resources. The development of clean, green technologies for energy production is a major challenge today mainly with respect to their use in mobile sources. Fortunately, many means of producing energy with much less damaging impacts on our environment are available.

The use of hydrogen as a substitute for the fossil fuels constitutes a relevant way of reducing greenhouse-gas emissions and improving air quality, especially in highly congested urban areas. Hydrogen is an environmentally clean fuel that

* *Corresponding author*. Tel./fax: +54 221 4210711.
E-mail addresses: bengoajf@quimica.unlp.edu.ar, bengoajf@yahoo.com.ar (J.F. Bengoa).
http://dx.doi.org/10.1016/j.ijhydene.2014.06.076
0360-3199/Copyright © 2014, Hydrogen Energy Publications, LLC. Published by Elsevier Ltd. All rights reserved.

appears to be a solution for use both in internal-combustion engines and in feeding fuel cells for stationary and mobile applications, with that gas already being the primary energy source for fuel cells [1].

An environmentally clean production of hydrogen is possible through the electrolysis of water by means of energy sources that are renewable (e. g., solar energy). This process, however, is not economically profitable because of the current energy costs. The new ecology-friendly technologies for hydrogen production point to biomass as the best energy feedstock. For this purpose, research on the production of hydrogen from the reforming of alcohols by catalysis has strongly increased in recent years. Alcohols are also convenient to store and transport [2]. For example, bio-ethanol—produced industrially from sugar cane, corn, or cereal fermentation—is an especially renewable fuel with low toxicity and high energy density.

Several authors have studied the steam reforming of ethanol. Freni el al [3,4]. found that Rh/Al_2O_3 produced hydrogen with a low ethylene content. Liguras et al. [5] reported a good activity and high stability for Ni/Al_2O_3 catalysts in the same process, whereas Fierro et al. [6] and Nishiguchi et al. [7] have focussed on the catalytic behavior of Ni/Cu and Cu/CeO_2.

In addition, different oxides have been used as catalysts in the ethanol-hydrotreatment process. Llorca et al [8] studied this synthesis using MgO, γ-Al_2O_3, SiO_2, TiO_2, V_2O_5, ZnO, La_2O_3, CeO_2, and Sm_2O_3 as catalysts and obtained the most promising results with ZnO. Barroso et al. [9] observed that if a bulk catalyst based on Ni–Zn–Al was used, the increase of Ni loading produced an enhancement in the selectivity for hydrogen, but an increasing amount of CO production was also obtained. Sánchez-Sánchez et al. [10], however, obtained a low selectivity for CO with an average selectivity for hydrogen at approximately 60% using Ni supported on Al_2O_3 modified with Ce, Mg, Zr, and La. Finally, Muroyama et al. [11] observed that ethanol reforming carried out on $NiFe_2O_4$ and $NiMn_2O_4$ catalysts produced a lower activity and hydrogen selectivity as a result of carbon deposition.

In recent years, fuel-cell development has led up to the point of investigating CO-free hydrogen production. The hydrogen for fuel cells is obtained through three catalytic steps: 1) ethanol steam reforming, 2) the water–gas-shift reaction, and 3) the selective oxidation of CO (i. e., via the so-called CO-PROX process) [12]. The development of a catalyst with a high hydrogen production and the simultaneous capability of consuming in a single step the CO produced as the by-product is therefore of extreme interest. To avoid multi-step processes, Remiro et al. [13] used a Ni/α-Al_2O_3 catalyst at 923 K and achieved total ethanol conversion and no carbon deposition. Horminella and coworkers [14] propose a two stages iron based catalyst methodology that implied higher temperature too to reach low CO in the final mixture products.

To that end the aim of the present work was to study the catalytic behavior of maghemite (γ-Fe_2O_3) and magnetite (Fe_3O_4) with respect to ethanol hydrotreatment at 673–758 K, atmospheric pressure, and a constant molar ratio H_2O/ethanol of 9/1 in order to produce H_2 with a low content of CO. A high H_2O/ethanol ratio was used to simulate the mixture arising from biomass treatment. However, in order to use this hydrogen for a fuel cell it would be necessary to decrease the water content previously.

Hematite (α-Fe_2O_3) was discarded as a catalyst because of its very low activity [15].

Material and methods

Catalyst preparation

Maghemite (γ-Fe_2O_3) and magnetite (Fe_3O_4) were obtained through a sol–gel method [16]. An aqueous solution of NH_4OH (30%, w/w) was added to a solution of $Fe(NO_3)_3.9H_2O$ in water (40%, w/v) up to pH = 9.8. The solid thus obtained was washed and centrifuged (at 2000 rpm for 5 min) in NH_4CH_3COO solution (5%, w/v) a total of five times then dried to constant weight in an oven at 333 K. The resulting solid was denoted IHA (i. e., iron-hydroxy-acetate).

The IHA was calcined at 690 K for 2 h in a stream of N_2 (100 cm^3/min) at a heating rate of 10 K/min. The iron oxide thus obtained was denoted m(f). The samples of this solid used in the reactions were indicated as m(673), m(713), or m(758); where the numbers refer to the catalytic test temperatures.

A fraction of m(f) was calcined for 2 h, at 573 K in a stream of air (150 cm^3/min) at a heating rate of 2.3 K/min. The iron oxide obtained was termed g(f). The samples of this solid used in the reactions were accordingly denoted g(673), g(713), or g(758); where the numbers indicate the catalytic test temperatures.

Catalyst characterization

The solids were characterized by N_2 adsorption at 77 K, X-ray diffraction (XRD), Mössbauer spectroscopy at 298 K (MS), diffuse-reflectance spectroscopy (DRS), and thermogravimetric-analysis (TGA).

The textural properties of specific surface area (S_g) and pore diameter (Dp), were measured in the Micromeritics equipment ASAP 2020 V1.02 E.

All XRD patterns were measured using a Phillips PW170 diffractometer with Cu Kα radiation, between a $2\theta = 20–70^\circ$ at steps of 0.02° and a counting time of 2 s/step.

The Mössbauer spectra at room temperature (RT) were obtained in transmission geometry with a 512-channel constant-acceleration spectrometer. A source of ^{57}Co in Rh matrix of a nominal 50 mCi was used. The velocity calibration was performed against a 12 μm-thick α-Fe foil. All isomer shifts (δ) cited here refer to this standard. The Mössbauer spectra were evaluated through the use of a fitting program named Recoil Spectral Analysis [17] under the assumption of Lorentzian lines. The spectra were folded to minimize geometric effects.

DRS uv–visible spectra within the 200–800 nm range were recorded in a CINTRA 20 spectrophotometer with an integrated sphere. The spectra were referenced against $BaSO_4$ powder.

TGA on a Shimadzu TGA-50 instrument was carried out in order to determine the surface-carbon deposition onto the

catalysts used. The samples were heated at 10 K/min from RT to 1173 K in an air stream of 20 cm^3/min. Before each assay, the solids were purged with a stream of He.

Activity and selectivity measurements

Measurements of activity and selectivity were carried out in a fixed-bed reactor containing 260 mg of fresh catalyst in each run at atmospheric pressure and with H_2O/CH_3CH_2OH at a molar ratio of 9/1, a total flow of 0.020 cm^3/min, and a space velocity (LHSV) of 2 h^{-1}. The reaction mixture was preheated and evaporated before its reactor inlet; which was operated at 673, 713, and 758 K, for 120 min. Before the start and after the completion of the reaction a N_2 stream (10 cm^3/min, overnight) was flushed through the reactor to prevent changes in the catalyst species.

The liquid products of the reaction were condensed in a cold trap during 120 min. The total liquid quantity was analyzed by gas chromatography with a FID detector on a DB-WAX capillary column in a Varian STAR 3400 CX chromatograph. The permanent gas phase was stored in a water filled burette inverted inside a container with water. The total gas volume collected during 120 min was measured with the burette. The gaseous mixture was analyzed by gas chromatography with a TCD detector on a Chromosorb 102 packed column, and with a FID detector on a GS-GASPRO capillary column, in a Konik HRGC 3000C chromatograph.

In all experiments, the gas flows were controlled using mass flow meters with an error of 1% full scale and the temperatures were measured with a precision of ±2K. Besides, in the activity tests, the error of the flow (ethanol + water) was of 1% and the chromatographic errors were of about 5%.

Results and discussion

Characterization of fresh catalysts

Fig. 1 shows the XRD patterns of the fresh catalysts. The diffractograms indicate the presence of maghemite (γ-Fe_2O_3) and/or magnetite (Fe_3O_4) according to the respective PDF numbers of 39-1346 and 19-0629. Both patterns are quite similar, containing the same peaks. The only difference detected was the presence of two peaks of extremely low intensity at $2\theta = 23.7$ and 26.1°. Consequently, this technique was found not to be able to distinguish between the two species with certainty.

The crystallite sizes for m(f) and g(f) were obtained from XRD line-profile analysis through the use of a Gaussian function in order to fit the integral breadth, after subtracting the maximum strain [18]. Table 1 shows the resulting values. The crystallite diameter in the m(f) sample proved to be of the same order (91 nm) as in the g(f)—i.e., 81 nm—within experimental error.

Table 1 includes the S_g of the solids, where the g(f) sample is seen to have a lower S_g than the m(f). This difference could be attributed to the sintering process involving the thermal oxidation of m(f) to produce g(f).

Fig. 2 shows the pore-size distribution obtained from N_2-adsorption measurements. The oxide m(f) has a narrow pore-size distribution with an average radius of 18 nm, whereas g(f)

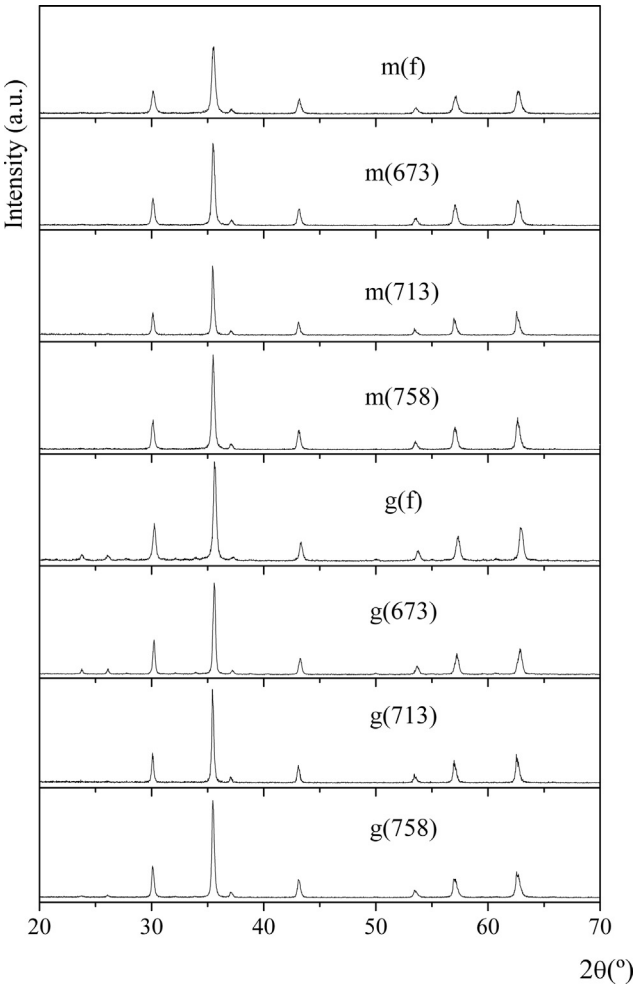

Fig. 1 – XRD patterns of the fresh and used catalysts.

contains a broad distribution with a mean radius of 6.5 nm. These differences could likewise be attributed to the sintering process mentioned above.

Fig. 3 shows the DRS spectra of m(f) and g(f) within the range 200–800 nm. Though both spectra were complex since the samples absorbed the radiation throughout the entire range of wavelengths, the curves were fitted through the use of six and seven Gaussian functions for the m(f) and g(f) catalysts, respectively. The parameters (position, full line-width

Table 1 – Specific surface area and crystallite diameter of the fresh and used catalysts.

Catalyst	S_g (m^2/g)	$D_{Crystallite}$ (nm)
m(f)	29 ± 3	91 ± 9
m(673)	20 ± 2	73 ± 7
m(713)	12 ± 1	87 ± 9
m(758)	21 ± 2	89 ± 9
g(f)	19 ± 2	81 ± 8
g(673)	13 ± 1	108 ± 11
g(713)	9 ± 1	147 ± 15
g(758)	6 ± 1	133 ± 13

S_g: specific surface area (BET).
$D_{Crystallite}$: crystallite diameter.

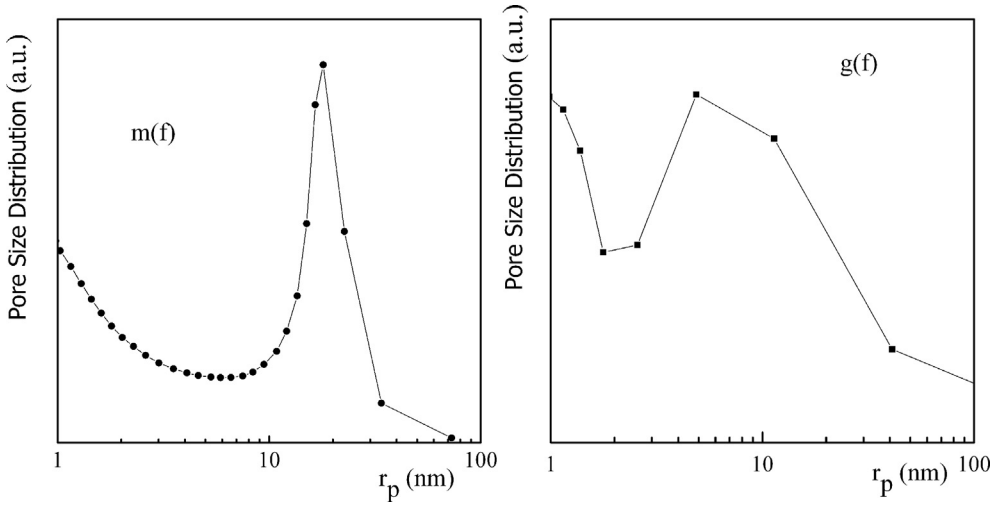

Fig. 2 – Pore size distribution of the fresh catalysts obtained from N_2-adsorption measurements.

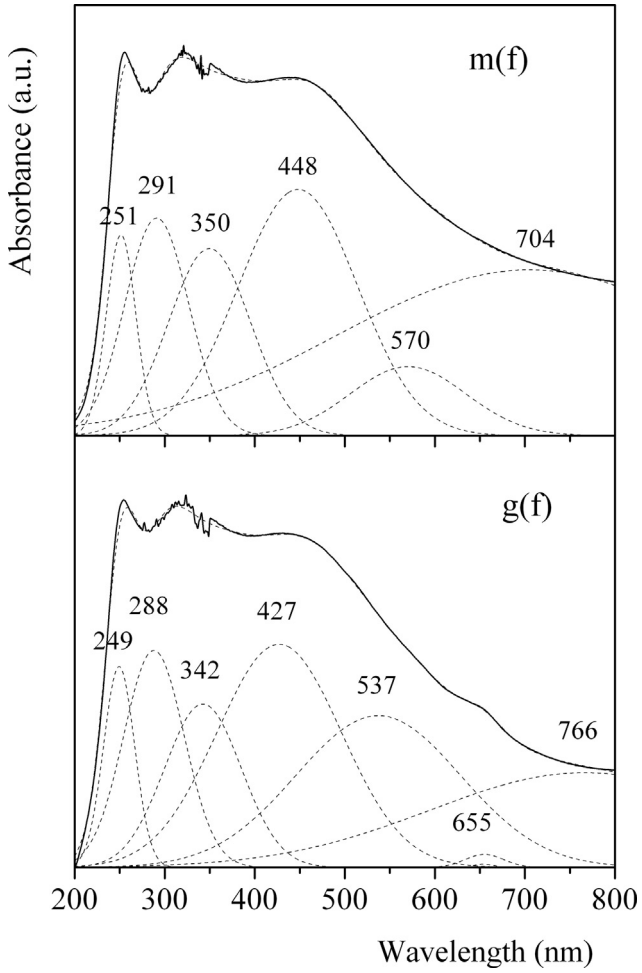

Fig. 3 – DRS spectra of fresh catalysts. UPPER PANEL: catalyst m(f); LOWER PANEL: catalyst g(f). The dashed lines are the computer-fitted curves.

at half-height, and area) were kept free for the fitting. The analysis was carried out on the basis of four specific absorption regions in both spectra according to He et al. [19]:

Region 1: 200–400 nm
Region 2: 400–600 nm
Region 3: 600–750 nm
Region 4: >750 nm

The ligand-metal charge-transfer transitions and the contributions of two d–d Fe^{3+} ligand field transitions make up Region 1. Region 2 is considered to be the result of a possible overlapping of the pair excitation processes with ligand-field transitions and charge-transfer band tails. Regions 3 and 4 are assigned to other Fe^{3+} d–d transitions. These uv–visible spectra, although characteristic of iron oxides, did not permit a precise identification of the species in each sample. Therefore, we needed to look for another spectroscopic technique in order to identify the present phases. For that purpose we resorted to Mössbauer spectroscopy at RT. Fig. 4a and b shows the Mössbauer spectra of the two solids. One sextet is present in the g(f) spectrum, whereas the spectrum for m(f) contains two sextets partially overlapped. From the hyperfine parameters obtained as a result of the fitting process (Tables 2 and 3), Fe_3O_4 was identified in m(f) with a stoichiometry of $Fe_{2.91}O_4$ and γ-Fe_2O_3 likewise in g(f) [20]. In the m(f) spectrum, signals corresponding to Fe^{3+} and $Fe^{\text{“}2.5+\text{”}}$—located in magnetite tetrahedral and octahedral sites, respectively—were identified [20]. The average signal assignable to the Fe^{2+} and the Fe^{3+} located in adjacent octahedral sites is presented as $Fe^{\text{“}2.5+\text{”}}$. Since at temperatures higher than 260 K a fast electron exchange (hopping) between both ions occurs, the Mössbauer spectroscopy records only one average oxidation state. The stoichiometry of m(f) was determined from the following expression [21]:

$$X = \frac{2 - 1.1 \times R}{6 + 4.945 \times R}$$

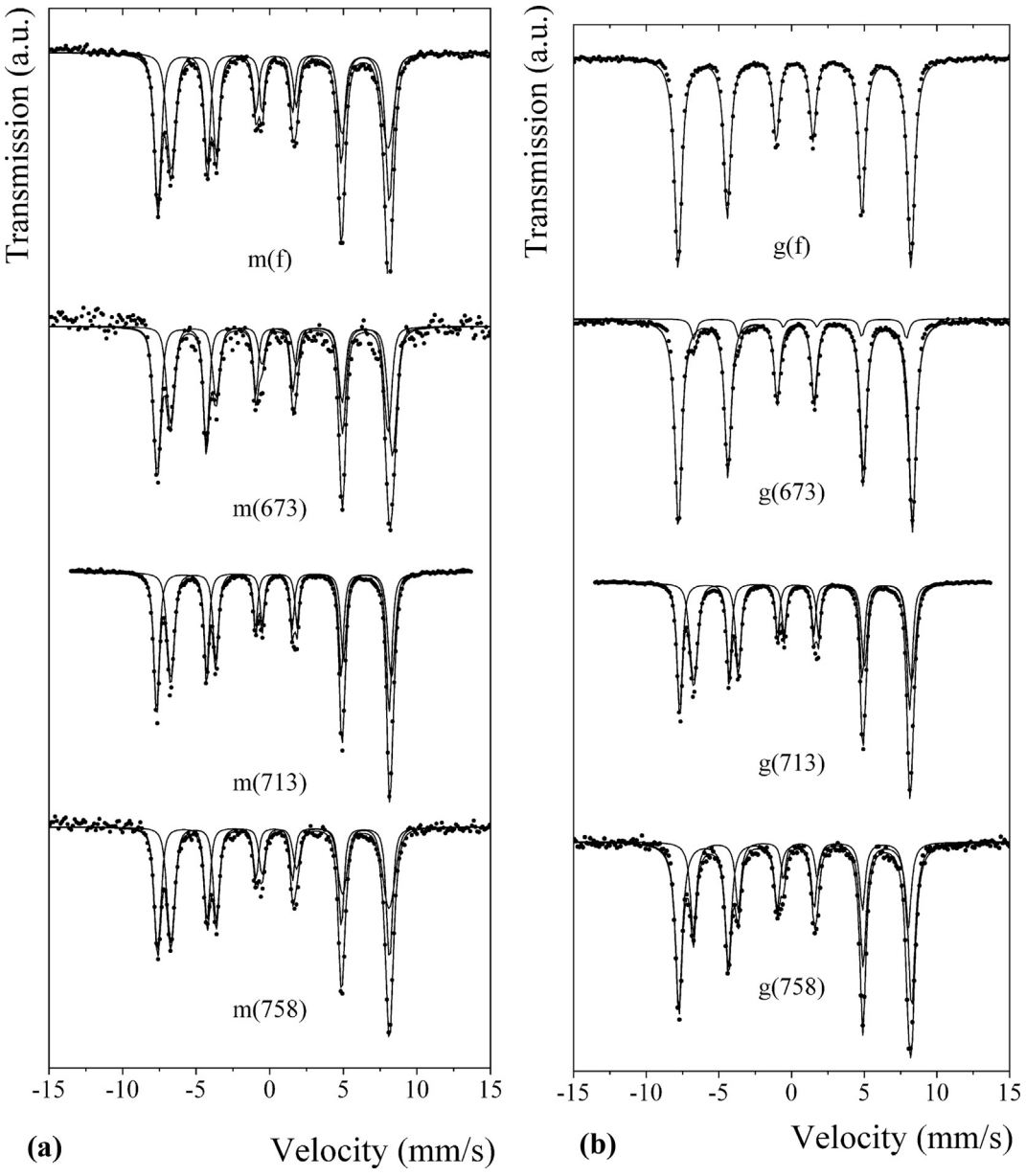

Fig. 4 – a: Mössbauer spectra of catalysts m(f), m(673), m(713) and m(758) at room temperature. b: Mössbauer spectra of catalysts g(f), g(673), g(713) and g(758) at room temperature.

where:

$$R = \frac{\text{Relative population of } Fe^{\}2,5+\}} \text{ in octahedral sites}}{\text{Relative population of } Fe^{3+} \text{ in tetrahedral sites}}$$

$X =$ oxidation parameter according with $Fe_{3-x}O_4$ formula

The species identified in g(f) indicated that the oxidation of m(f) had led to a complete oxidation of the magnetite.

Activity and selectivity measurements

The average activity and selectivity results were evaluated after two hours of reaction time at the three temperatures with both catalysts. Fig. 5 shows the average conversion levels reached for both catalysts, with the conversion being defined as:

$$X(\%) = \frac{\text{inlet ethanol moles} - \text{outlet ethanol moles}}{\text{inlet ethanol moles}} \times 100$$

It is remarkable that at the lowest temperature (673 K), g(673) showed a significantly higher conversion value (≈30%) than m(673). This point will be discussed below. When, however, the reaction temperature was increased from 673 to 713 K, this difference became reversed: m(713) reached a total conversion of ethanol, whereas the value for g(713) was about 90%. Finally, both catalysts attained a total conversion at 758 K.

Table 2 – Mössbauer hyperfine parameters of the catalysts m(f), m(673), m(713) and m(758) at 298 K.

Species	Parameter	m(f)	m(673)	m(713)	m(758)
Fe^{3+} ions in A sites of Fe_3O_4	H(T)	48.7 ± 0.1	49.6 ± 0.1	48.99 ± 0.01	48.9 ± 0.1
	δ (mm/s)	0.29 ± 0.01	0.33 ± 0.02	0.25 ± 0.01	0.29 ± 0.01
	2ε (mm/s)	−0.02 ± 0.01	0.01 ± 0.01	−0.07 ± 0.01	−0.03 ± 0.01
	%	51 ± 1	58 ± 1	51 ± 1	48 ± 1
$Fe^{"2.5+"}$ ions in B sites of Fe_3O_4	H(T)	45.7 ± 0.1	45.8 ± 0.1	46.51 ± 0.02	46.0 ± 0.1
	δ (mm/s)	0.66 ± 0.01	0.64 ± 0.02	0.72 ± 0.01	0.68 ± 0.01
	2ε (mm/s)	0.01 ± 0.01	0.00 ± 0.01	0.10 ± 0.01	0.02 ± 0.01
	%	49 ± 1	42 ± 1	49 ± 1	52 ± 1

H: hyperfine magnetic field in Tesla; δ: isomer shift (all the isomer shifts are referred to α-Fe at 298 K); 2ε: quadrupole shift.
A sites: tetrahedral sites.
B sites: octahedral sites.

Table 4 summarizes the selectivity values, where selectivity is defined as:

$$S_i = \frac{\text{moles of product i}}{\text{total moles of products}} \times 100$$

The selectivity values for H_2 proved to be nearly the same for both catalysts (within experimental error) over the entire temperature range studied. Since the conversion values are different under these conditions (Fig. 5), within the conversion range obtained, H_2 selectivity apparently did not depend on the degree of ethanol conversion, it remained consistently between 63.6 and 68.1% (Table 4). Moreover, at the highest reaction temperature (758 K) the selectivity values for all products with g(758) as catalyst are seen to be quite similar to the values obtained for m(758). Furthermore, the two other main products detected in all assays were acetone and CO_2, though CO, methane, ethane, ethylene, and the hydrocarbons C3–C5 were detected in all experiments in minor quantities as well. In all instances, carbon deposition was not observed, as confirmed by TGA measurements (not shown), on the used catalysts at the three temperatures.

Ethanol steam reforming can be schematized by the following overall reaction:

1) $CH_3CH_2OH + 3H_2O \rightarrow 2\,CO_2 + 6H_2$
Ethanol steam reforming

To explain, however, the values of selectivity obtained with the different catalysts, the inclusion of the contribution of the following reactions was necessary, all of which conversions were stated in the Gauss-Jordan (G-J) methodology [22]:

2) $CH_3CH_2OH \rightarrow CH_3CHO + H_2$ (Ethanol dehydrogenation)

3) $2CH_3CHO \rightarrow CH_3COCH_3 + CO + H_2$
(Addition and decarbonylation)

4) $CO + H_2O \rightarrow CO_2 + H_2$ (WGS)

In addition, the reaction mass balance was completed with the following reactions:

5) $CO_2 + 4H_2 \rightarrow CH_4 + 2H_2O$

6) $2CO_2 + 7H_2 \rightarrow C_2H_6 + 4H_2O$

7) $2CO_2 + 6H_2 \rightarrow C_2H_4 + 4H_2O$

Table 3 – Mössbauer hyperfine parameters of the catalysts g(f), g(673), g(713) and g(758) at 298 K.

Species	Parameter	g(f)	g(673)	g(713)	g(758)
γ-Fe_2O_3	H(T)	49.7 ± 0.1	50.0 ± 0.1	–	–
	δ (mm/s)	0.32 ± 0.01	0.38 ± 0.01	–	–
	2ε (mm/s)	0.01 ± 0.01	0.01 ± 0.01	–	–
	%	100 ± 1	93 ± 3	–	–
Fe^{3+} ions in A sites of Fe_3O_4	H(T)	–	–	49.02 ± 0.01	49.7 ± 0.1
	δ (mm/s)	–	–	0.25 ± 0.01	0.38 ± 0.01
	2ε (mm/s)	–	–	−0.068 ± 0.002	−0.03 ± 0.01
	%	–	–	49 ± 1	68 ± 3
$Fe^{"2.5+"}$ ions in B sites of Fe_3O_4	H(T)	–	45.4 ± 0.1	46.46 ± 0.01	45.8 ± 0.1
	δ (mm/s)	–	0.70 ± 0.02	0.72 ± 0.01	0.72 ± 0.01
	2ε (mm/s)	–	0.00*	0.091 ± 0.003	0.02 ± 0.01
	%	–	7 ± 2	51 ± 1	32 ± 2

H: hyperfine magnetic field in Tesla; δ: isomer shift (all the isomer shifts are referred to α-Fe at 298 K); 2ε: quadrupole shift; *Parameter held fixed in fitting.
A sites: tetrahedral sites.
B sites: octahedral sites

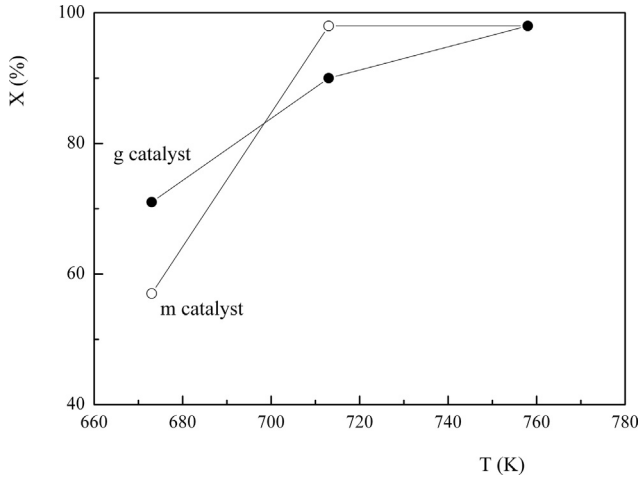

Fig. 5 – Average conversion levels of ethanol into products reached for the two catalysts after two hours of reaction at the three indicated temperatures. The percent conversion (X) is plotted vs. the temperature in K. Open circles, the m catalyst; closed circles, the g catalyst.

8) $3CO_2 + 10H_2 \rightarrow C_3H_8 + 6H_2O$

9) $3CO_2 + 9H_2 \rightarrow C_3H_6 + 6H_2O$

10) $4CO_2 + 12H_2 \rightarrow C_4H_8 + 8H_2O$

11) $4CO_2 + 13H_2 \rightarrow C_4H_{10} + 8H_2O$

12) $5CO_2 + 16H_2 \rightarrow C_5H_{12} + 10H_2O$

Table 4 – Selectivity results of the catalysts at the different reaction temperatures.

Si	T (K)					
	m catalyst			g catalyst		
	673	713	758	673	713	758
SH_2	65.8	67.2	64.5	68.1	63.9	63.6
SCO	3.9	1.5	1.4	2.2	1.0	1.4
SCO_2	9.2	12.2	13.7	11.7	11.0	13.4
SCH_4	0.1	0.3	0.8	0.1	0.2	0.6
SC_2H_6	1.8	1.2	1.6	1.7	1.5	1.6
SC_2H_4	1.0	1.1	1.2	1.1	1.2	1.2
SC_3H_8	0	0.1	0.1	0	0	0.1
SC_3H_6	0	0.2	0.3	0.2	0.3	0.3
SC_4H_{10}	0	0	0	0	0	0.1
SC_4H_8	0	0	0.4	0	0.1	0.2
SC_5H_{12}	0	0.1	0	0	0	0
SCH_3CHO	3.9	0.2	0.2	3.6	0.7	0.2
SCH_3COCH_3	14.3	15.9	15.8	11.3	20.1	17.3

T (K): reaction temperature.

In the application of the above-mentioned methodology in order to determine the total composition of the system, twelve components had to be measured. Except for the water, all the other components were measured. Thus, the carbon balance was confirmed experimentally. As an example, Table 5 shows the molar balances obtained with m(758) as catalyst. The outlet moles calculated were similar to those measured. The higher dispersion was seen with CO_2 and H_2. As mentioned above, the gas phase was isolated after being passed through an inverted burette filled with water. Therefore, some CO_2 remains solved in water. However, its solubility does not justify by itself the difference between the CO_2 moles calculated and experimental ones. Taking into account that the water quantity was not experimentally evaluated, and CO_2 and H_2 are involved in several reactions producing water, errors in water estimation could lead to differences between the moles of CO_2 and H_2 calculated and experimental ones. By contrast, the calculated and experimental molar outlets for acetone and all the hydrocarbons shown in the table are in complete agreement since each of these compounds participates in only one reaction. From stoichiometric analysis by means of the G-J methodology, hydrogen is produced mainly via ethanol dehydrogenation with both catalysts and at the three temperatures. This would imply a large acetaldehyde production. The presence of only small amounts of acetaldehyde (Table 4) would indicate that the rate of reaction 3) would be higher than that of reaction 2). Acetaldehyde was not detected at 758 K. In addition, in all instances, the reactions 5–12) show the lower reaction advance.

The CO concentrations achieved with both catalysts do not exceed 3400 ppm over the entire temperature range and become as low as 1000 ppm for g(713). As mentioned in the Introduction, in the H_2-production process for use in fuel cells, the catalytic ethanol reforming is followed by the water-gas-shift (WGS) reaction, carried out in two stages. In the first, the high-temperature WGS (HT-WGS) reaction occurs in a reactor that operates at approximately 673 K. The CO

Table 5 – Calculated and experimental molar balances obtained with catalyst m(758).

m(758)			
Compound	Experimental $Moles_{in}$	Experimental $Moles_{out}$	Calculated $Moles_{out}$
CH_3CH_2OH	11.26	0.18	0.23
H_2O	101.34	–	96.73
H_2	–	18.44	20.62
CO	–	0.39	0.39
CO_2	–	3.92	5.33
CH_4	–	0.24	0.24
C_2H_6	–	0.46	0.46
C_2H_4	–	0.33	0.33
C_3H_8	–	0.04	0.04
C_3H_6	–	0.08	0.08
C_4H_8	–	0.11	0.11
CH_3CHO	–	0.05	0.05
CH_3COCH_3	–	4.54	4.54

Experimental $Moles_{in}$: fed moles quantified by GC.
Experimental $Moles_{out}$: outlet moles quantified by GC.
Calculated $Moles_{out}$: moles calculated from the G-J methodology.

concentration obtained in that step is about 10,000 ppm. The gases emerging from this reactor are fed to a second reactor operating at around 473 K. This second step, referred to as the low-temperature WGS (LT-WGS) reaction, provides a stream of products containing about 1000 ppm of CO [12]. On the basis of these details, we can conclude that both catalysts used in the present study provide promising results in terms of the relatively low content of CO achieved with only a single reactor in a so-called one-pot synthesis.

Used-catalyst characterization

In order to find a correlation between the catalysts' solid properties and catalytic performances we carried out a characterization of the solids after the reactions.

Table 1 shows the textural properties of the used catalysts. After reacting, the g catalysts had progressively decreased S_g values with increased reaction temperatures. This pattern could be related to a sintering process that produced the observed increase in the crystallite diameter up to 713 K, after which temperature the crystallite size remained approximately constant. In contrast, the used m catalysts showed no clear pattern in the S_g values, while the crystallite size remained nearly constant.

From the XRD patterns of the catalysts m(673), m(713), and m(758) depicted in Fig. 1 we found that all of three exhibited the same peaks as were seen with m(f). These results allowed us to conclude that during the catalytic reaction the solid structure remained unaltered despite the changes in the composition of the reaction atmosphere at the three temperatures studied.

In contrast, analyzing the diffractograms of the three g catalysts, we observed that when the reaction temperature increased, all the peaks except the ones at $2\theta = 23.7$ and 26.1° remained at the same angle. These latter peaks were also not present in g(713) and g(758). Therefore, the diffractograms of the solids used at the two higher temperatures were seen to be in total agreement with those of m(f). From these observations we concluded that when the reaction temperature exceeded 673 K, the contact of maghemite with the reaction products, reduced it, leading to magnetite. This was subsequently verified by Mössbauer spectroscopy since, as stated earlier, XRD was unable to distinguish conclusively between magnetite and maghemite.

The Mössbauer spectra of m(673), m(713), and m(758) in Fig. 4a contained two sextets partially overlapped on the negative-velocity side that were completely overlapped within the positive-velocity range. The Mössbauer parameters (Table 2) indicated the presence of magnetite in all instances [20]. The different reaction temperatures, however, produced a slight change in the stoichiometry of the resultant magnetite. Whereas in m(f) the composition is $Fe_{2.91}O_4$; in the solids m(673), m(713), and m(758) the stoichiometry was $Fe_{2.87}O_4$, $Fe_{2.91}O_4$,, and $Fe_{2.93}O_4$, respectively. This redistribution would indicate that at 673 K the fresh solid underwent an oxidation. This process was then reversed when the reaction temperature was increased, so that at 758 K the solid composition became closer to that of stoichiometric magnetite than in the fresh catalyst. These transformations could be explained on the basis of the catalyst's contact with both reducing (H_2, CO) and oxidizing (H_2O, CO_2) gases, with the presence of a redox atmosphere being dependent on the relative concentration of those two types of gases within the thermal process.

In the Mössbauer spectrum of g(673) in Fig. 4b, a shoulder is present on the right side of the first peak of the sextet at the negative velocities that becomes more clearly defined with the increased reaction temperatures of g(713) and g(758). All the spectra were fitted with two sextets. In these latter two catalysts the hyperfine parameters (Table 3) were typical of magnetite [20]. In contrast, in catalyst g(673) the hyperfine parameters corresponded to γ-Fe_2O_3 (the more intense signal) and $Fe^{\text{“}2.5+\text{”}}$, where the latter could indicate the presence of these ions isolated on the surface of the catalyst particles. These $Fe^{\text{“}2.5+\text{”}}$ ions, associated with the Fe^{3+} of the maghemite would lead to a more open structure than a pure magnetite. As a consequence, in this conditions the activity of g(673) result higher than m(673). It is important to remark that there is no pure maghemite in any catalytic test.

When the reaction temperature was higher than 673 K, all the maghemite became converted to magnetite. This conversion could explain the similar catalytic behavior obtained with m(758) and g(758).

The magnetite present in g(713) had a stoichiometry of $Fe_{2.92}O_4$, identical to that of m(713). In g(758), however, a slight oxidation could have occurred since the stoichiometry found was $Fe_{2.82}O_4$. Since the catalyst was exposed to a high temperature in a greatly reductive atmosphere, the occurrence of an oxidation reaction was highly improbable. Moreover, since the degree of conversion and product distribution are very similar with m(758) and g(758) as catalysts, an incorrect handling during the cooling and passivation steps might have caused the oxidation.

Conclusions

We have demonstrated that both the catalysts magnetite ($Fe_{2.91}O_4$) and maghemite (γ-Fe_2O_3) exhibit satisfactory activity for use in ethanol hydrotreatment. Nevertheless, magnetite would appear to be better than maghemite since the latter is converted into magnetite at temperatures higher than 713 K because of the reducing atmosphere. Moreover, maghemite undergoes a sintering process with a decrease in the specific surface area available for catalysis.

The catalysts are active in both hydrogen production—with selectivity values for H_2 of 63–68%—and CO removal through the WGS reaction, achieving CO-concentration values at the reactor outlet ranging from 1000 to 3400 ppm. The CO content of the product stream is lower than those reported in the literature for other catalytic systems, thus being quite low for an ethanol-reforming process without the inclusion of further purification reactors loaded with specific catalysts for the oxidation of CO to CO_2 through the WGS reaction.

Since magnetite promoted with Cr is the industrial catalyst for the WGS, in which CO is consumed, we speculate that an improved catalyst design such as the one described here will enable the replacement of a process that currently covers three stages—one of ethanol reforming and two of WGS—by one that involves a *one-pot* reaction. Finally, this report contributes to the better use of biomass, usually burned very

inefficiently, producing the generation of hazardous substances for the environment.

Acknowledgments

The authors acknowledge the support for this work to the Consejo Nacional de Investigaciones Científicas y Técnicas, Comisión de Investigaciones Científicas de la Provincia de Buenos Aires and Universidad Nacional de La Plata. Dr. Donald F. Haggerty, a retired career investigator and native English speaker, edited the final version of the manuscript.

REFERENCES

[1] Laborde MA, Rubiera González F. In: Laborde MA, Rubiera González F, editors. La energía del hidrógeno". Buenos Aires: CYTED; 2010. pp. 7–10.
[2] Brown LF. A comparative study of fuels for on-board hydrogen production for fuel-cell-powered automobiles. Int J Hydrogen Energy 2001;26:381–97.
[3] Freni S, Maggio G, Cavallaro S. Ethanol steam reforming in a molten carbonate fuel cell: a thermodynamic approach. J Power Sources 1996;62(1):67–73.
[4] Freni S, Cavallaro S, Mondello N, Saparo L, Frusteri F. Production of hydrogen for MC fuel cell by steam reforming of ethanol over MgO supported Ni and Co catalysts. Catal Commun 2003;4:259–68.
[5] Liguras DK, Kondarides DI, Verykios XE. Production of hydrogen for fuel cells by steam reforming of ethanol over supported noble metal catalysts. Appl Catal B Environ 2003;43:345–54.
[6] Fierro V, Klouz V, Akdim O, Mirodatos C. Oxidative reforming of biomass derived ethanol for hydrogen production in fuel cell applications. Catal Today 2002;75:141–4.
[7] Nishiguchi T, Matsumoto T, Kanai H, Utani K, Matsumura Y, Shen W-Y, et al. Catalytic steam reforming of ethanol to produce hydrogen and acetone. Appl Catal A General 2005;279:273–7.
[8] Llorca J, Ramirez de la Piscina P, Sales J, Homs N. Direct production of hydrogen from ethanolic aqueous solutions over oxide catalysts. Chem Commun 2001:641–2.
[9] Barroso MN, Gomez MF, Arrúa LA, Abello MC. Hydrogen production by ethanol reforming over NiZnAl catalysts. Appl Catal A General 2006;304:116–23.
[10] Sánchez-Sánchez MC, Navarro RM, Fierro JLG. Ethanol steam reforming over $Ni/M_xO_y–Al_2O_3$ (M=Ce, La, Zr and Mg) catalysts: Influence of support on the hydrogen production. Int J Hydrogen Energy 2007;32:1462–71.
[11] Muroyama H, Nakase R, Matsui T, Eguchi K. Ethanol steam reforming over Ni-based spinel oxide. Int J Hydrogen Energy 2010;35:1575–81.
[12] Mariño F, Ayastuy JL. In: Laborde MA, Rubiera González F, editors. "La energía del hidrógeno". Buenos Aires: CYTED; 2010. pp.99–115.
[13] Remiro A, Valle B, Oar-Arteta L, Aguayo AT, Bilbao J, Gayubo AG. Hydrogen production by steam reforming of bio-oil/bio-ethanol mixtures in a continuous thermal-catalytic process. Int J Hydrogen Energy 2014;39:6889–98.
[14] Hormilleja E, Durán P, Plou J, Erguido J, Peña JA. Hydrogen from ethanol by steam iron process in fixed bed reactor. Int J Hydrogen Energy 2014;39:5267–73.
[15] Fellenz N, Alvarez AM, Bengoa JF, Gallegos NG, Cagnoli MV, Marchetti SG. Estabilidad térmica y química de catalizadores de óxidos de Fe en el hidrotratamiento de etanol. In: Proc.. of XVIII Simposio Iberoamericano de Catálisis, Isla Margarita, Venezuela; 2002. pp. 2230–5.
[16] Rangel M, do Carmo, Galembeck F. Magnetite formation on silica and alumina. J Catal 1994;145:364–71.
[17] Lagarec K, Rancourt DG. Mossbauer spectral analysis software. Dep. of Phys. University of Otawa Version 1.0; 1998.
[18] Rathore KS, Patidar DP, Janub Y, Saxenaa NS, Sharmaa K, Sharmaa TP. Structural and optical characterization of chemically synthesized ZnS nanoparticles. Chalcogenide Lett 2008;5(6):105–10.
[19] He YP, Miao YM, Li CR, Wang SQ, Cao L, Xie SS, et al. Size and structure effect on optical transitions of iron oxide nanocrystals. Phys Rev B 2005;71:125411–9.
[20] Vandenberghe RE, De Grave E, Landuydt C, Bowen LH. Some aspects concerning the characterization of iron oxides and hydroxides in soils and clays. Hyperfine Interact 1990;53: 175–95.
[21] van der Kraan AM. Mössbauer effect studies of surface ions of ultrafine a-Fe_2O_3 particles. Phys Status Solid (a) 1973;18:215–26.
[22] Atkinson KE. An introduction to numerical analysis. 2nd ed. New York: John Wiley & Sons; 1989.